TU Delft

Delft University of Technology

Thickness optimization algorithm to improve multilayer diffractive optical elements performance

Laborde, Victor ; Loicq, J.J.D.; Hastanin, Juriy ; Habraken, Serge

DOI
10.1364/AO.474107

Publication date
2023

Document Version
Final published version

Published in
Applied Optics

Citation (APA)
Laborde, V., Loicq, J. J. D., Hastanin, J., & Habraken, S. (2023). Thickness optimization algorithm to improve multilayer diffractive optical elements performance. *Applied Optics*, *62*(3), 836-843. https://doi.org/10.1364/AO.474107

Important note
To cite this publication, please use the final published version (if applicable).
Please check the document version above.

Copyright
Other than for strictly personal use, it is not permitted to download, forward or distribute the text or part of it, without the consent of the author(s) and/or copyright holder(s), unless the work is under an open content license such as Creative Commons.

Takedown policy
Please contact us and provide details if you believe this document breaches copyrights.
We will remove access to the work immediately and investigate your claim.

This work is downloaded from Delft University of Technology.
For technical reasons the number of authors shown on this cover page is limited to a maximum of 10.

Green Open Access added to TU Delft Institutional Repository

'You share, we take care!' - Taverne project

https://www.openaccess.nl/en/you-share-we-take-care

Otherwise as indicated in the copyright section: the publisher is the copyright holder of this work and the author uses the Dutch legislation to make this work public.

applied optics

Thickness optimization algorithm to improve multilayer diffractive optical elements performance

Victor Laborde,[1,*] Jérôme Loicq,[1,2] Juriy Hastanin,[1] and Serge Habraken[1]

[1]Centre Spatial de Liege, Avenue du Pré-Aily, 4031 Angleur, Belgium
[2]Faculty of Aerospace Engineering, Delft University of Technology, Kluyverweg 1, 2629 HS Delft, The Netherlands
*Corresponding author: victor.laborde@uliege.be

Received 25 August 2022; revised 12 December 2022; accepted 19 December 2022; posted 20 December 2022; published 20 January 2023

The diffractive zone thicknesses of conventional diffractive optical elements (DOEs) are generally obtained using the thin element approximation (TEA). However, the TEA yields inaccurate results in the case of thick multilayer DOEs (MLDOEs). The extended scalar theory (EST) is an alternative thickness optimization method that depends on the diffractive order and the optimization wavelength. We developed an algorithm to research suitable EST input parameters. It combines ray-tracing and Fourier optics to provide a performance estimate for each EST parameter pair. The resulting "best" MLDOE designs for three different material combinations are analyzed using rigorous finite-difference time-domain. Compared to the TEA, the proposed algorithm can provide performing zone thicknesses. © 2023 Optica Publishing Group

https://doi.org/10.1364/AO.474107

1. INTRODUCTION

For monitoring purposes in the thermal infrared (IR) domain, dual-band instruments are often sufficient [1,2], provided they offer daily revisit time. This is achievable using constellations of small satellites, which sets the need for compact dual-band IR imagers. Two IR wave bands are considered, defined by the atmospheric IR windows: mid-wave IR (MWIR) from 3 to 5 μm and long-wave IR (LWIR) from 8 to 12 μm. The MWIR band is often shortened (4.4–5 μm) to avoid solar albedo contributions.

Refractive systems are rendered more compact when combined with extremely thin diffractive lenses. In addition, these diffractive optical elements (DOEs) very well compensate for the chromatic and thermal defocuses of refractive lenses. However, conventional monolayer DOEs cannot be used for dual-band IR applications since they can operate only within a narrow spectral band. High-order DOEs are a potential solution, considering the first diffractive order in LWIR and the second diffractive order in MWIR. Nevertheless, this causes a discontinuous chromatic focal shift, rendering the longitudinal chromatic aberration (LCA) correction difficult.

Another solution studied in this paper consists of an extended dual-band DOE called multilayer DOE (MLDOE). This optical component has been studied since 1997 [3]. As for monolayer DOEs, the thin element approximation (TEA) provides an analytical scalar approximation to describe an MLDOE's diffractive behavior, predicting very high performance [4–6]. Nonetheless, this approximation does not hold for thick elements [7]. By design, an MLDOE has a typical groove thickness 100 times higher than conventional DOEs, rendering the TEA inaccurate.

Alternative scalar theories have recently been researched to fill the gap between the TEA and rigorous numerical methods. The effective-area method applies geometric optics to sawtooth MLDOEs to model the "shadowing effect" and perform more accurate computations of diffraction efficiency [8,9]. The extended scalar theory (EST), introduced in [10] and recently applied to MLDOEs [11], combines the grating equation and Snell's law to optimize the profile of a DOE (reducing the shadowing effect). Finally, ray-tracing and Fourier optics have been combined to estimate MLDOE's optical performance at the focal plane [12] and provide a material selection method [13]. This concept is not new and has been used for the modeling and design of hybrid optical systems [14,15]. The optical performance of many MLDOE examples has been accurately retrieved using the finite-difference time-domain (FDTD) method [12,13]. It has been proven that these MLDOEs, designed with TEA thickness equations, had much lower performance than expected.

In this paper, we propose an algorithm to find suitable groove thickness for any MLDOE. This process is based on the EST (Section 2) and combines a ray-based phase model (called "ray model") with Fourier optics. According to the EST, the thickness of each MLDOE layer depends only on the diffractive order p and optimization wavelength λ_{opt}. Since there is no optimal way of choosing these parameters, to the authors' knowledge,

without using the TEA, the algorithm performs a parametric study to estimate an optimal pair (p, λ_{opt}). An MLDOE's optical performance is computed at its "best" focal plane and evaluated over the MWIR-LWIR wave bands using the Strehl ratio metric. The latter is retrieved using a free space Fourier optics propagator and a reliable scalar approximation of the MLDOE near field: the ray model (Section 3). This algorithm is applied in Section 5 for three MLDOE combinations, ensuing from the MLDOE material selection process introduced in [13]. As a result, a suitable EST input pair (p, λ_{opt}) allows for generating an "optimal" MLDOE profile design for each material combination. In Section 6, the validity of the proposed algorithm is analyzed by comparing the predicted optical performance with accurate FDTD simulations. The results are finally discussed in Section 7.

2. MLDOE EST DESIGN

This section recalls the EST, introduced in [10], and its application to MLDOEs [11]. The EST uses Snell's law of refraction to compute the so-called "shadowing factor" for a diffraction blazed grating. In opposition to the TEA, the EST considers finite DOE thickness, allowing to model the negative impact of the shadowing factor on diffraction efficiency. Consequently, a method to optimize any DOE's thickness based on its period and working order is described in [10]. By combining Snell's law of refraction and the grating equation, this method provides a grating thickness that reduces the shadowing effect.

Following this reasoning, alternative MLDOE layer thickness equations have been proposed [11]. They are based on the layout depicted in Fig. 1.

Following the Fig. 1 layout, we define n_1, n_g, and n_2 as the refractive indices of layer 1, the gap, and layer 2, respectively. Similar to a diffractive lens, the mth zone's aperture radius r_m and period size T_m are classically defined by

$$\begin{cases} r_m^2 = m r_1^2 = 2mf\lambda_d, \\ T_m = r_{m+1} - r_m, \end{cases} \tag{1}$$

where λ_d represents one of the two design wavelengths, and f is the associated MLDOE focal length. $\alpha_1 = H_1/T_m$ and $\alpha_2 = H_2/T_m$, with H_1 and H_2 the microstructure heights of layer 1 and 2, respectively. H_1 and H_2 are initially computed using the TEA, as described in [11,12]:

$$\begin{cases} H_1 = \dfrac{\lambda_2 A(\lambda_1) - \lambda_1 A(\lambda_2)}{B(\lambda_1)A(\lambda_2) - B(\lambda_2)A(\lambda_1)}, \\ H_2 = \dfrac{\lambda_1 B(\lambda_2) - \lambda_2 B(\lambda_1)}{B(\lambda_1)A(\lambda_2) - B(\lambda_2)A(\lambda_1)}, \end{cases} \tag{2}$$

where $A(\lambda) = n_2(\lambda) - n_g(\lambda)$, and $B(\lambda) = n_1(\lambda) - n_g(\lambda)$. The wavelengths λ_1 and λ_2 are MLDOE design wavelengths, defined in two distinct wave bands. The EST height calculation for the first layer is detailed in the following.

Equating the refractive and diffractive deviation angles leads to the layer height values $H_1^{EST}(T_m)$ and $H_2^{EST}(T_m)$, for each zone m of layers 1 and 2, respectively [11]:

$$\begin{cases} H_1^{EST}(T_m) = \dfrac{p_1\lambda_{opt}}{n_1\cos\theta_i - \sqrt{n_g^2 - \left(\frac{p_1\lambda_{opt}}{T_m} + n_1\sin\theta_i\right)^2}}, \\ H_2^{EST}(T_m) = \dfrac{p_2\lambda_{opt}}{\sqrt{n_2^2 - \left(\frac{(p_1+p_2)\lambda_{opt}}{T_m} + n_1\sin\theta_i\right)^2} - \sqrt{n_g^2 - \left(\frac{p_1\lambda_{opt}}{T_m} + n_1\sin\theta_i\right)^2}}. \end{cases} \tag{3}$$

The resulting MLDOE layer heights $H_1^{EST}(T_m)$ and $H_2^{EST}(T_m)$ depend on the chosen "optimization" wavelength λ_{opt} and on the chosen operating orders p_1 and p_2. Refractive indices in Eq. (3) are defined at λ_{opt}. Since this paper focuses on the on-axis MLDOE design and performance, $\theta_i = 0°$ is assumed in the following.

A major difference with the TEA arises since the EST heights are now period dependent. Consequently, each MLDOE diffractive zone m will have a unique thickness $H_{EST}(T_m)$. Equation (3) supposes that $p_1 + p_2 = 1$, which is imposed in this whole paper to ensure that the studied MLDOE designs are converging (first order).

The diffractive orders p_1 and p_2 are expressed in [11], based on the harmonic DOEs (HDOEs) theory [16,17]:

$$\begin{cases} p_1 = \frac{H_1}{\lambda_{opt}}[n_1(\lambda_{opt}) - n_g(\lambda_{opt})], \\ p_2 = \frac{H_2}{\lambda_{opt}}[n_2(\lambda_{opt}) - n_g(\lambda_{opt})] \\ \Rightarrow p_1 + p_2 = 1. \end{cases} \tag{4}$$

The relation $p_1 + p_2 = 1$ is ensured using the TEA heights definition of Eq. (2). Since Eq. (4) is based on HDOE's design equations, and therefore relies on the TEA, it might provide unreliable results (see Section 6).

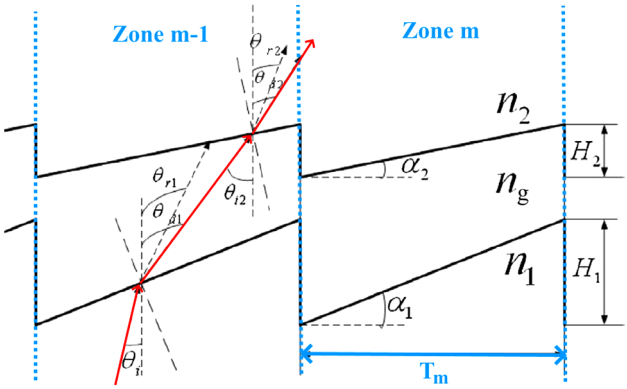

Fig. 1. Extended scalar theory applied to an MLDOE (adapted from [11]). The deviation angle θ_d is obtained using the local grating equation, while θ_r results from Snell's law. Initially, the layer heights H_1 and H_2 are constant, given by the TEA. EST alternative profile heights are obtained when $\theta_d = \theta_r$ for both layers. T_m is the mth zone period. The light trajectory is displayed in red.

3. MONOCHROMATIC STREHL RATIO SIMULATION

In this section, we recall a procedure to retrieve the Strehl ratio and the focal length of any MLDOE design. In the whole paper, the Strehl ratio at the best focal plane is used as the main MLDOE optical performance metric. This simulation process has been introduced in [12] and is depicted in Fig. 2.

The Strehl ratio retrieval procedure depicted in Fig. 2 combines near-field modeling (step 1) and free-space optical propagation (step 2). The latter revolves around the angular spectrum (AS) of plane waves [18,19]. Step 1 consists of modeling an MLDOE near field, using either the scalar approach

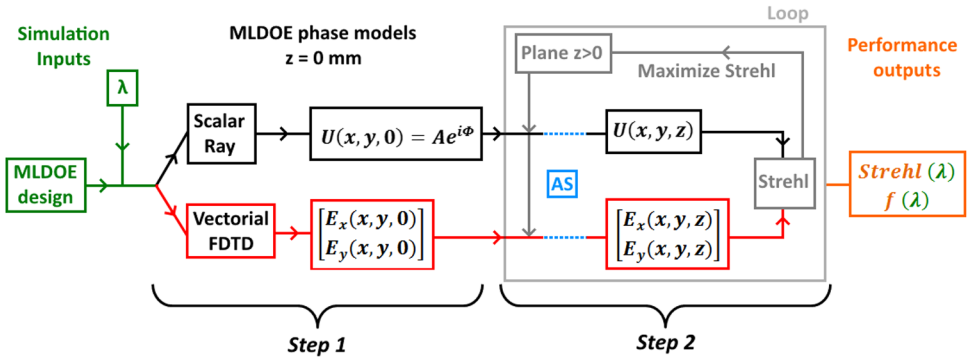

Fig. 2. Diagram showing the hybrid procedure used in this paper to retrieve the Strehl ratio and the focal length of any MLDOE design. This procedure is divided into two steps: (1) modeling the MLDOE near field and (2) using Fourier optics (angular spectrum, AS) in free space to retrieve the two above-mentioned outputs. Step 1 MLDOE field modeling involves two approaches: one is scalar (top black), based on ray-tracing and called "ray model" [12], while the other is vectorial (bottom red), based on the finite-difference time-domain method (FDTD).

named ray model [12] or the rigorous vectorial electromagnetic approach called the FDTD method.

The ray model uses ray-tracing to compute optical path differences, taking refraction effects into account. The impact of an MLDOE on a monochromatic plane wave is obtained in the near field through the calculation of an amplitude loss A_{ray} and a phase mask Φ_{ray} using the professional ray-tracing software ASAP NextGen [20]. The ray model provides a fast and tunable near-field phase and amplitude computation method. Consequently, it is used as an optimization tool in this paper. The ray model is a scalar approximation; therefore, this paper uses FDTD as a reference. Furthermore, this rigorous electromagnetic calculation method will serve as a verification tool since it requires high computation effort.

FDTD wave simulation is performed using OptiFDTD software [21]. Starting from a plane wave, a complex electric field is propagated numerically through the MLDOE. The circular symmetry of the problem is used to reduce the sampling effort needed. Adequate sampling has been studied in the worst-case scenario [12]: low f-number ($f/10$), high material index (germanium), and low wavelength ($\lambda = 4.4$ μm). Figure 3 shows the sampling convergence curve, obtained by computing the Strehl ratio at the focal plane, based on the built-in FDTD far-field calculator, for each sampling trial.

As a result of Fig. 3, the following sampling is selected: $N_x = 20000$ and $N_t = 5000$, which is sufficient even in a worst-case scenario. All FDTD simulations performed in this paper are therefore considered exact.

The procedure depicted in Fig. 2 takes an MLDOE design as input (i.e., periods T_m and thicknesses $H_{T_m}^{\text{EST}}$ for any zone m) and is purely monochromatic. The loop, displayed in gray, allows to precisely determine the best focal plane $f(\lambda)$. The input wavelength λ is called "simulation wavelength" and is unrelated to the previously defined optimization wavelength λ_{opt}.

The focal plane of an MLDOE is theoretically given by the following law, whose expression is the same as for standard DOEs [6]:

$$f_j(\lambda) = D\frac{F/\#}{j\lambda}, \tag{5}$$

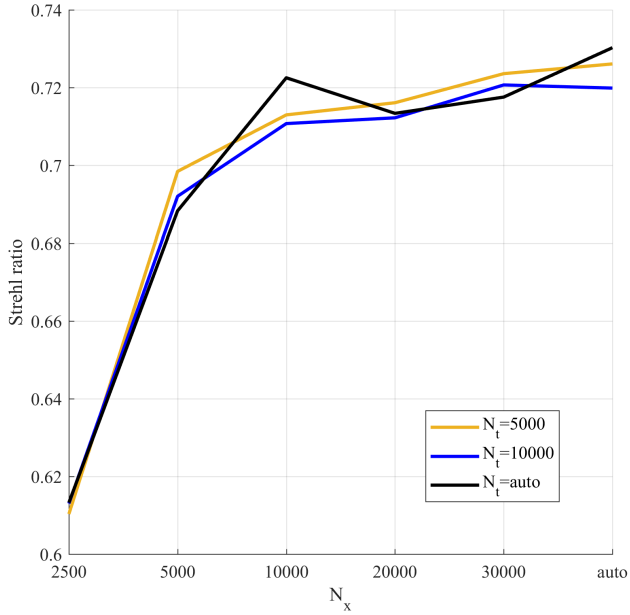

Fig. 3. FDTD sampling convergence curve. The metric associated with each sampling trial is the Strehl ratio, computed at the "best" focal plane. The sampling along the optical axis (N_z, δ_z), as well as radial and time sampling steps δ_x and δ_t, are automatically computed by the OptiFDTD software ("auto setup"). N_x is the number of samples in the radial dimension (perpendicular to wave propagation direction z), and N_t is the number of time steps.

where j is the diffractive order ($j = 1$ is considered in this paper).

However, since this law has been demonstrated using the TEA, it might be inaccurate for thick MLDOEs. Consequently, the best focal plane is considered unknown in this paper. Concentrating on the loop, displayed in gray in Fig. 2, each optical propagation to any plane $z > 0$ leads to a Strehl ratio. Therefore, the best focal plane $f(\lambda)$ is defined as the plane with the highest Strehl ratio output and is determined iteratively.

Finally, the Fig. 2 simulation procedure will be referred to as "monochromatic ray simulation" when the ray model is used or as "monochromatic FDTD simulation" when FDTD is used instead.

4. MLDOE PROFILE OPTIMIZATION ALGORITHM

In this section, an algorithm to determine suitable layer thicknesses for any MLDOE is developed. This algorithm researches the "best" EST input pair (order p_1 and optimization wavelength λ_{opt}) that leads to the most performing MLDOE design. According to Eqs. (2) and (3), the choice of the pair (p_1, λ_{opt}) greatly impacts the resulting MLDOE layer heights and the output performance.

Recall that the diffractive orders of both layers are linked ($p_1 + p_2 = 1$) and that Eq. (4) relates p_1 to λ_{opt}. Since this relation is based on the HDOE theory [16,17], which involves the TEA, we perform two parametric studies. On one hand λ_{opt} is the only design variable [p_1 is defined according to Eq. (4)] while, on the other hand, p_1 and λ_{opt} vary independently.

We arbitrarily fix the design parameters used in the next sections of this paper. The aperture diameters are set to $D = 10$ mm for a total of $N_{zones} = 10$ diffractive zones. The f-number is set to 15 (at $\lambda = 8$ µm) and the design wavelengths are selected in the middle of both MWIR and LWIR wave bands: $\lambda_1 = 4.7$ µm and $\lambda_2 = 10$ µm. The period T_m of each zone m is defined in Eq. (1). The algorithm is divided into two steps: choosing an EST input pair (p_1, λ_{opt}) leading to a certain MLDOE thickness distribution and estimating its optical performance using the monochromatic ray simulation at many wavelengths (Fig. 2). For each pair (p_1, λ_{opt}) (i.e., each EST MLDOE geometries), the Strehl ratio is estimated using the ray model at the best focal plane of each wavelength and then averaged to provide the polychromatic Strehl ratio (PSR), defined in Eq. (6). Each PSR value is tied to a certain MLDOE thickness design, and a full PSR map is obtained by browsing over all potential values of (p_1, λ_{opt}). For each material combination, a PSR map is retrieved and provides the "optimal" design pair (p_1, λ_{opt}), according to the ray model. Figure 4 describes the proposed thickness optimization algorithm.

The procedure depicted in Fig. 4 provides a mapping of the PSR. According to Eqs. (3) and (3), each pair (p_1, λ_{opt}) provides a specific MLDOE design (thicknesses H_2^{EST} and H_1^{EST}) that can be evaluated using the PSR. It is defined in this paper over a wave band Δ_λ:

$$\mathrm{PSR}_{\Delta_\lambda}(p_1, \lambda_{opt}) = \frac{1}{\lambda_{max} - \lambda_{min}} \int_{\lambda_{min}}^{\lambda_{max}} \mathrm{Strehl}(\lambda;\, p_1, \lambda_{opt})\mathrm{d}\lambda, \tag{6}$$

where λ_{max} and λ_{min} represent the boundary wavelengths of the wave band Δ_λ. The total IR PSR (called "PSR" in Fig. 4) is the weighted sum of two PSRs, one calculated in MWIR and the other in LWIR:

$$\mathrm{PSR}(p_1, \lambda_{opt}) = \frac{1}{2}[\mathrm{PSR}_{MWIR}(p_1, \lambda_{opt}) + \mathrm{PSR}_{LWIR}(p_1, \lambda_{opt})]. \tag{7}$$

Considering an MLDOE design [i.e., a pair (p_1, λ_{opt})], the PSR is obtained using the monochromatic ray simulation (Fig. 2, ray model) for multiple MWIR-LWIR wavelengths (green loop).

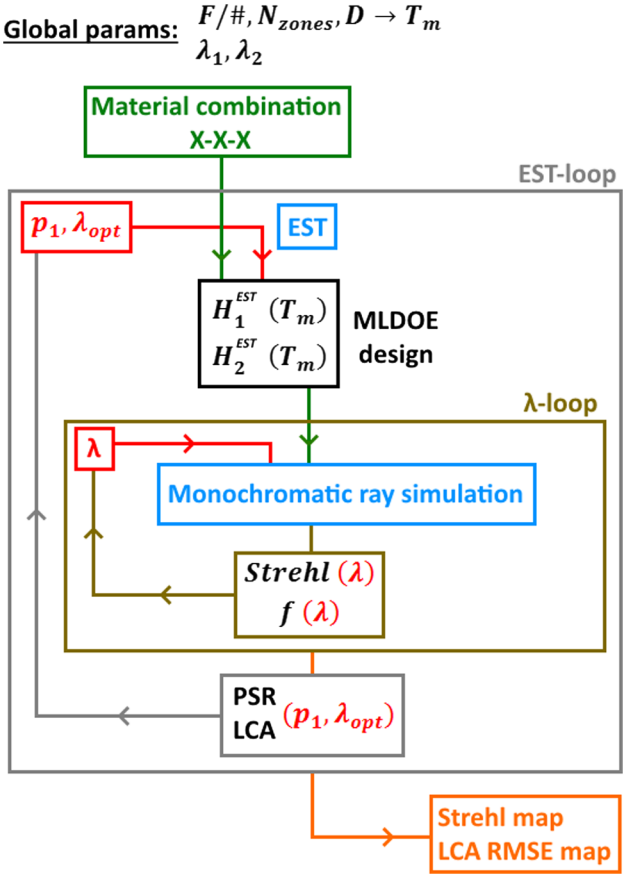

Fig. 4. Diagram describing the proposed MLDOE thickness optimization algorithm. It is divided into two loops and searches the "best" EST input doublet (p_1, λ_{opt}). A set of layer materials and a pair (p_1, λ_{opt}) defines an "MLDOE design." The green loop involves the ray model and Fig. 2 diagram. It is performed over the MWIR-LWIR wave bands. At the end of the loop, the polychromatic Strehl ratio (PSR) is obtained for each pair (p_1, λ_{opt}). This process is repeated in the main loop (gray) for each value of (p_1, λ_{opt}), resulting in either a PSR curve [if Eq. (4) is applied] or a PSR two-dimensional map. This output map (or curve) is specific for each MLDOE material combination, given the above-mentioned global parameters.

5. RESULTS OF THE OPTIMIZATION ALGORITHM

In this section, the proposed algorithm's results (Fig. 4) are detailed. This EST input selection process is applied to three particular MLDOE combinations, ensuing from the MLDOE material selection process introduced in [13]. The IRG24-air-IRG27, ZnS-air-Ge, and IRG24-IRG27-AgCl combinations have been selected regardless of their potential manufacturing issues. The IRG24 and IRG27 materials belong to SCHOTT's chalcogenide family [22]. They are "softer" than ZnS and Ge, with lower refractive indices and can potentially be molded. Since two-layer DOEs (i.e., air-gap MLDOEs) are more likely to be manufactured, we have selected an "all chalcogenide" solution (IRG27-air-IRG27), a more "classical" solution (ZnS-air-Ge) and finally, a three-layer solution (IRG24-IRG27-AgCl) made of "soft" materials. It has been shown in [13] that these MLDOE combinations performed relatively poorly (see Section 6), especially for IRG24-air-IRG27 and ZnS-air-Ge.

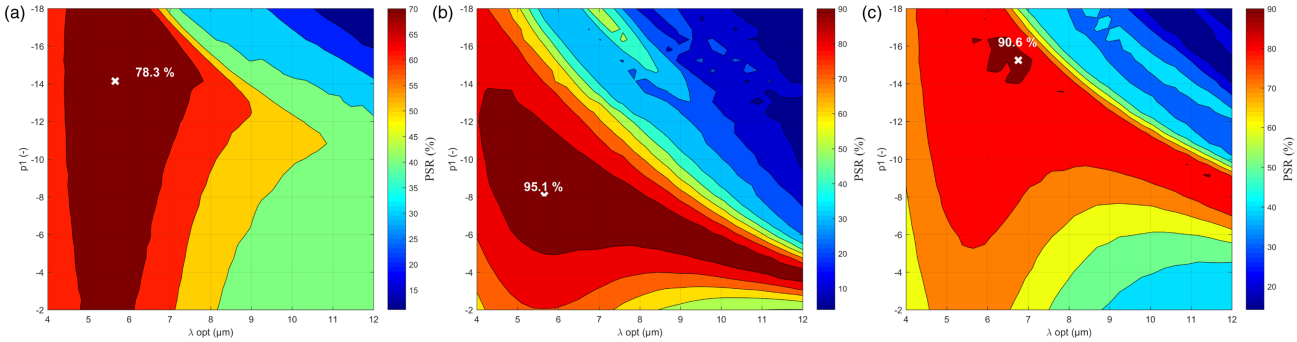

Fig. 5. PSR maps for the three selected MLDOE combinations: (a) IRG24-air-IRG27, (b) IRG24-IRG27-AgCl, and (c) ZnS-air-Ge. These maps result from the application of Fig. 4 algorithm, with order p_1 and wavelength λ_{opt} both variable and independent. A white cross displays the maximal PSR value. λ_{opt} varies within the MWIR-LWIR wave bands, while $|p_1|$ is kept relatively small to obtain "thinner" layers.

Table 1. Algorithm Design Results Assuming Both (p_1, λ_{opt}) Are Variable and Independent[a,b]

MLDOE Unit	p_1 -	p_2 -	λ_{opt} μm	$H_1^{EST}(T_1)$ μm	$H_1^{EST}(T_{10})$ μm	H_1^{TEA} μm	$H_2^{EST}(T_1)$ μm	$H_2^{EST}(T_{10})$ μm	H_2^{TEA} μm	PSR %
IRG24-air-IRG27	−14	15	5.7	60	57	262	64	60	297	74
IRG24-IRG27-AgCl	−8	9	5.7	247	237	255	110	112	115	95
ZnS-air-Ge	−15	16	6.8	81	76	121	36	35	52	91

[a]Their selected values correspond to the maximum PSR for all three MLDOE combinations in Fig. 5. $H_{1,2}^{EST}(T_1)$ and $H_{1,2}^{EST}(T_{10})$ are the resulting layer heights, corresponding, respectively, to the central zone (period T_1) and extreme zone (period T_{10}).
[b]The TEA heights are computed for both layers, based on Eq. (2), for comparison.

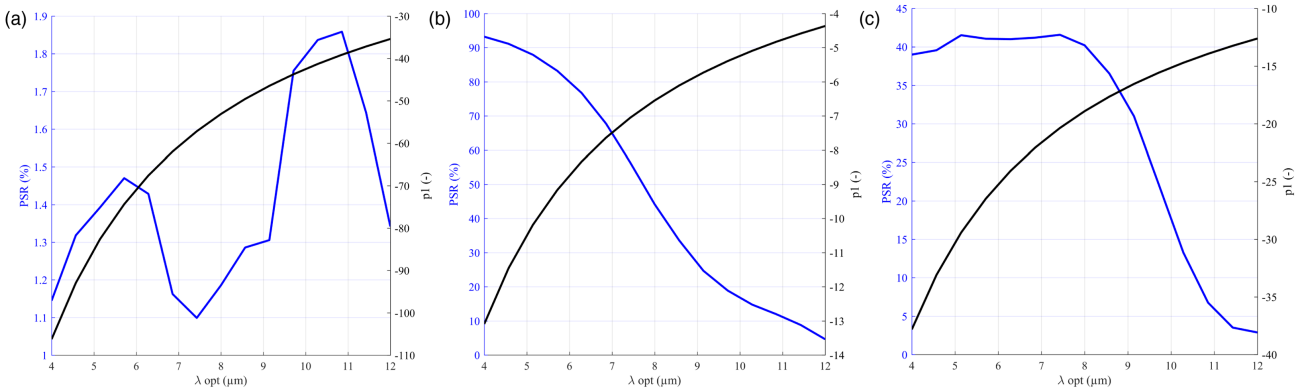

Fig. 6. PSR and diffractive order p_1 curves for various optimization wavelengths λ_{opt}, for the three selected MLDOE combinations: (a) IRG24-air-IRG27, (b) IRG24-IRG27-AgCl, and (c) ZnS-air-Ge. The PSR curves (blue, left axis) result from the application of Fig. 4 algorithm, assuming that the order p_1 (black curves, right axis) is defined by Eq. (4). λ_{opt} varies within the MWIR-LWIR wave bands.

The result of the proposed optimization algorithm is displayed in Fig. 5, assuming that p_1 and λ_{opt} are variable and independent. The PSR maps depicted in Fig. 5 provide "optimal" pairs (p_1, λ_{opt}) for all three selected MLDOEs. The results are shown in Table 1.

The next study relies on Eq. (4) to define the diffractive order p_1 [11]. Only λ_{opt} is variable, leading to the one-dimensional curve outputs of Fig. 6. The PSR curves shown in Fig. 6 provide different (p_1, λ_{opt}) pairs than in Fig. 5. The diffractive order values obtained by Eq. (4) are rather different, especially for the IRG24-air-IRG27 and ZnS-air-Ge combinations. For these two designs, the maximal PSR output values, according to the ray model, are also much lower than in Fig. 5, particularly for IRG24-air-IRG27. The "optimal" results of the proposed algorithm, in this case, are displayed in Table 2.

When p_1 and λ_{opt} are variable, the proposed algorithm can find profile heights that lead to high MLDOE PSRs for each of the three studied MLDOEs. It is no more the case for the IRG24-air-IRG27 and ZnS-air-Ge combinations when Eq. (4) is applied. Their PSR values drop drastically, meaning that the design in Eq. (4) is unreliable, at least according to the ray model. Since the latter is a scalar approximation, a rigorous electromagnetic method such as FDTD must be used to validate the presented results.

6. FDTD RESULTS VALIDATION

In this section, the "optimal" EST input pairs (p_1, λ_{opt}) obtained in Section 5 are used. The term "map" optimization refers to Fig. 5, considering independently variable order

Table 2. Algorithm Design Results Assuming Variable λ_{opt} [a,b,c,d]

MLDOE Unit	p_1 -	p_2 -	λ_{opt} µm	$H_1^{EST}(T_1)$ µm	$H_1^{EST}(T_{10})$ µm	H_1^{TEA} µm	$H_2^{EST}(T_1)$ µm	$H_2^{EST}(T_{10})$ µm	H_2^{TEA} µm	PSR %
IRG24-air-IRG27	−39	40	11	260	144	262	264	151	297	1.8
IRG24-IRG27-AgCl	−13	14	4	253	242	255	115	118	115	93
ZnS-air-Ge	−19	20	8	124	106	121	53	50	52	40

[a] p_1 follows Eq. (4).
[b] The selected (p_1, λ_{opt}) values correspond to the maximum PSR for each of the three MLDOE combinations.
[c] $H_{1,2}^{EST}(T_1)$ and $H_{1,2}^{EST}(T_{10})$ are the resulting layer heights, corresponding, respectively, to the central zone (period T_1) and extreme zone (period T_{10}).
[d] The TEA heights are computed for both layers, based on Eq. (2), for comparison.

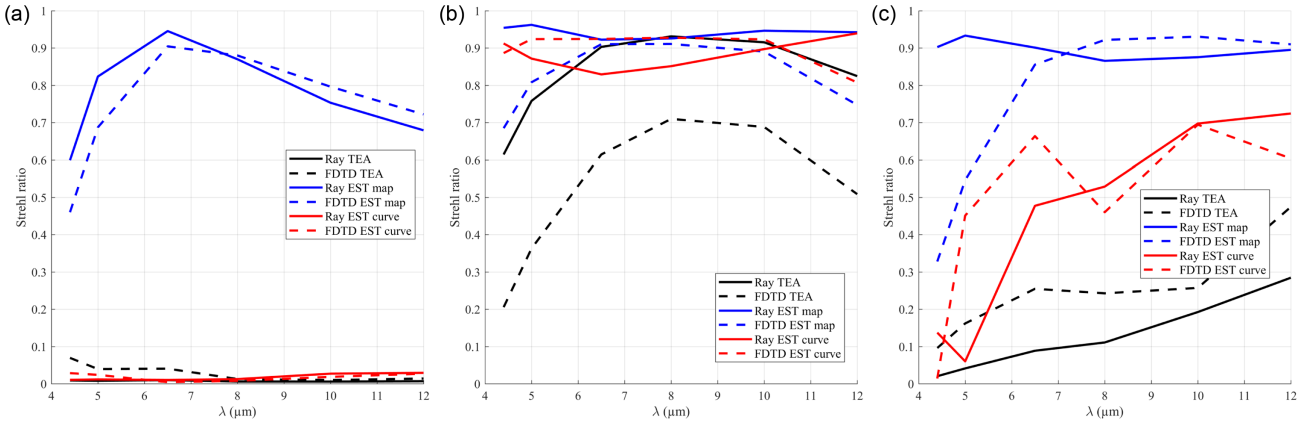

Fig. 7. Strehl ratio for various wavelengths in the MWIR-LWIR wave bands, considering the three studied MLDOE configurations: (a) IRG24-air-IRG27, (b) IRG24-IRG27-AgCl, and (c) ZnS-air-Ge. For each combination, six curves are depicted: The continuous curves are made with the ray model, whereas the dashed curves are obtained with FDTD (reference). The "map" optimization, "curve" optimization and "TEA profile" (no optimization) results are displayed in blue, red, and black, respectively. The black curves originate from [13].

and wavelength, whereas "curve" optimization refers to Fig. 7, where Eq. (4) is applied.

Each MLDOE design's performance is retrieved over various wavelengths in the MWIR-LWIR wave bands, using the "monochromatic FDTD simulation" procedure described in Fig. 2. This process is accurate since both FDTD and the AS provide exact fields (as long as the sampling is fine enough).

Figure 7 refers to "Ray TEA" and "FDTD TEA" when the Strehl ratio is, respectively, obtained by the ray model and FDTD, assuming TEA MLDOE profile heights [Eq. (2)]. Similarly, Fig. 7 refers to "Ray EST map," "FDTD EST map," "Ray EST curve," and "FDTD EST curve" when the Strehl ratio is obtained with the ray model or FDTD, assuming map or curve optimization.

The results shown in Fig. 7 are very variable, depending on the MLDOE combination. For example, in Fig. 7(a), the proposed algorithm can significantly increase the Strehl ratio. Inversely, the design in Eq. (4) is unreliable since it provides a very low Strehl ratio.

The IRG24-IRG27-AgCl combination studied in Fig. 7(b) already has a relatively high TEA Strehl ratio. The proposed algorithm still finds a better design, though the ray model is overly optimistic, especially in MWIR. If Eq. (4) is used to define the order [Fig. 6(b)], the Strehl ratio increases to 90% (red dashed curve).

Finally, Fig. 7(c) shows that the algorithm allows to reach a 90% Strehl ratio in LWIR (blue dashed curve), but the ray model does not predict the high MWIR Strehl ratio decrease. Applying Eq. (4) provides an "average" design, with a Strehl ratio higher than in the TEA case (although still very low in MWIR) but lower than using the map [Fig. 5(c)].

The MWIR divergence between the ray model and FDTD is displayed in Fig. 8 for the ZnS-air-Ge combination, using the monochromatic MLDOE simulation process at $\lambda = 4.4$ µm and recording the irradiance at many propagation planes $z > 0$.

In Fig. 8, the ray model cannot predict the second diffractive order, degrading the best focal plane performance. As a result, the ray model overestimates the Strehl ratio for this wavelength, which impacts the EST parameter selection and leads to a sub-optimal design choice.

Finally, the LCA is computed over the MWIR-LWIR wave bands to provide a more design-oriented evaluation. Thereby, in addition to the Strehl ratio, the monochromatic MLDOE simulation (Fig. 2) also retrieves the best focal length $f(\lambda)$. In this paper, the LCA is defined as

$$\mathrm{LCA} = f(\lambda) - f(\lambda = 8\ \mu\mathrm{m}), \tag{8}$$

and the theoretical LCA is deduced from Eq. (5). The LCA is displayed in Fig. 9 for all three MLDOE combinations and both map and curve optimizations.

Considering the map optimization in Fig. 9, all three MLDOEs have slowly varying LCAs with slopes different from the theoretical one. The ray model and FDTD provide near-identical LCA curves. In the case of curve optimization, except for the IRG24-IRG27-AgCl design, the resulting LCA

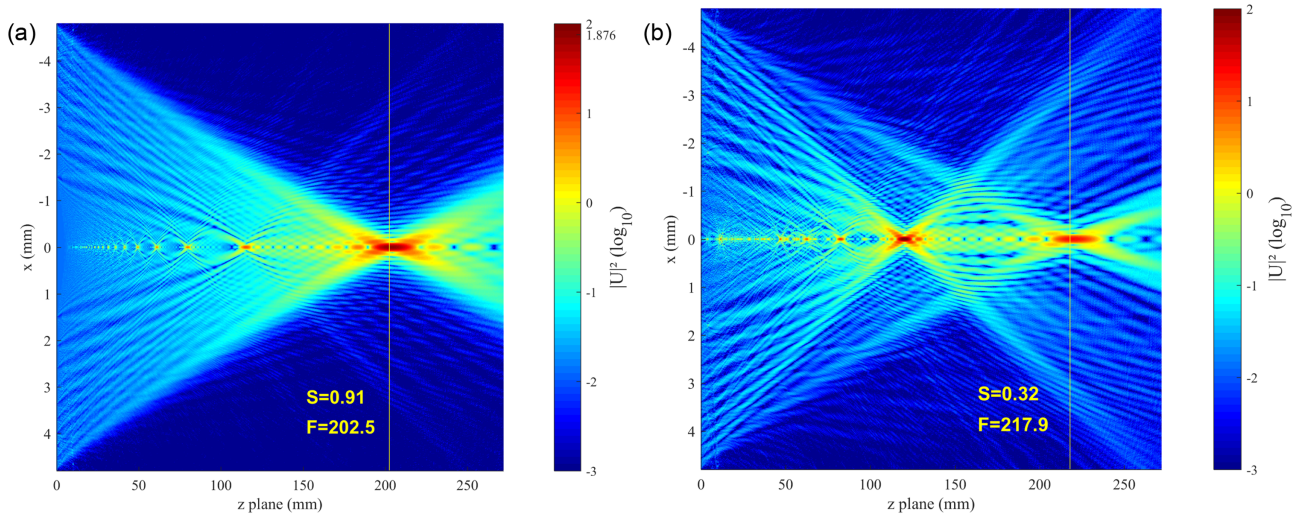

Fig. 8. Irradiance along the optical axis for the ZnS-air-Ge combination, using the setup given in Table 1 at a simulation wavelength of 4.4 μm. This simulation is made with the "monochromatic MLDOE simulation" process considering the (a) ray model and (b) FDTD (reference). The focal length (F) and Strehl ratio (S) are displayed in yellow and correspond to the values obtained in Fig. 7 at this wavelength (blue curves). Only FDTD can model the second diffractive order, generating a much lower Strehl ratio than the approximate ray model.

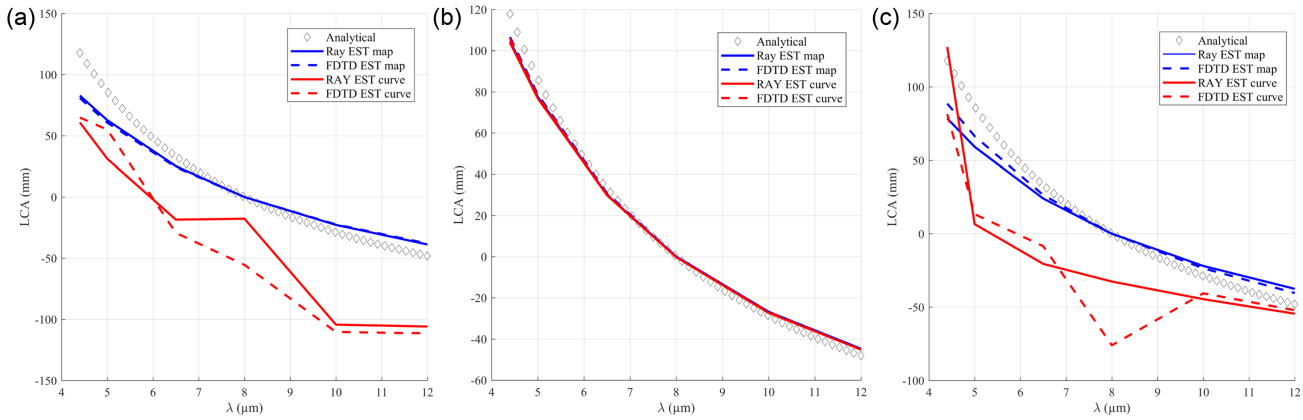

Fig. 9. LCA over the MWIR-LWIR wave bands, considering the three studied MLDOE configurations: (a) IRG24-air-IRG27, (b) IRG24-IRG27-AgCl, and (c) ZnS-air-Ge. For each combination, five curves are depicted: continuous curves are made with the ray model, whereas the dashed curves are obtained with FDTD (reference). The "map" optimization, "curve" optimization, and theoretical LCA are displayed in blue, red, and black diamonds, respectively.

curves are much steeper, with high variations. FDTD and ray model curves still have similar variations but display higher divergences.

7. CONCLUSION

It is shown in Figs. 7 and 9 that curve optimization is unreliable. Since Eq. (4) is based on the HDOE theory (i.e., TEA), it cannot provide suitable MLDOE profile heights for every MLDOE combination. Depending on the considered materials, it can generate highly performing designs [Figs. 7(b) and 9(b)] as well as poorly performing profiles [Figs. 7(a) and 9(a)]. For that reason, the proposed algorithm must primarily be used with independently variable order and optimization wavelength.

Based on the approximate ray model, the algorithm has enhanced the optical performance of all three MLDOE designs compared to their initial Strehl ratios (black curves in Fig. 7). The resulting LCA curves are very accurate and slowly varying. Consequently, the studied MLDOEs can be combined with refractive systems to correct the chromatic focal shift, assuming that the focal lengths are well selected.

However, as shown in Fig. 7(a)–7(c), the Strehl ratio accuracy of the ray model, and, by extension, of the proposed algorithm, is variable. For instance, it is relatively accurate in Fig. 7(a), but highly overestimates the MWIR Strehl ratio of the ZnS-air-Ge configuration in Fig. 7(c). As shown in Fig. 8, a second diffractive order that the ray model does not predict largely impacts the beam shape and degrades the Strehl ratio of the first diffractive order.

In addition, map optimization does not ensure that the EST parameter choice is optimal since it provides a lower performance in Fig. 7(b) than in curve optimization. In conclusion, at least for the presented MLDOE configurations, the proposed algorithm can provide an MLDOE thickness design that

enhances the TEA performance. The latter does not necessarily provide the "best" solution and is less accurate than FDTD, which must always be used for validation. The best focal plane position determination is precise in all studied cases.

Disclosures. The authors declare no conflicts of interest.

Data availability. No data were generated or analyzed in the presented research.

REFERENCES

1. J. A. Sobrino, F. Del Frate, M. Drusch, J. C. Jimenez-Munoz, P. Manunta, and A. Regan, "Review of thermal infrared applications and requirements for future high-resolution sensors," IEEE Trans. Geosci. Remote Sens. **54**, 2963–2972 (2016).
2. J. A. Sobrino, F. Del Frate, M. Drusch, J. C. Jimenez Munoz, and P. Manunta, *Review of High Resolution Thermal Infrared Applications and Requirements: The Fuegosat Synthesis Study* (Springer, 2013), Vol. **17**.
3. Y. Arieli, S. Noach, S. Ozeri, and N. Eisenberg, "Design of diffractive optical elements for multiple wavelengths," Appl. Opt. **37**, 6174–6177 (1998).
4. C. Fan, Z. Wang, L. Lin, M. Zhang, and H. Fan, "Design of infrared telephoto-optical system with double layer harmonic diffractive element," Chin. Phys. Lett. **24**, 1973 (2007).
5. C. Xue, Q. Cui, T. Liu, Y. Liangliang, and B. Fei, "Optimal design of multilayer diffractive optical element for dual wavebands," Opt. Lett. **35**, 4157–4159 (2010).
6. V. Laborde, J. Loicq, and S. Habraken, "Modeling infrared behavior of multilayer diffractive optical elements using Fourier optics," Appl. Opt. **60**, 2037–2045 (2021).
7. G. Greisukh, G. Danilov, E. Ezhov, S. Stepanov, and B. Usievich, "Comparison of electromagnetic and scalar methods for evaluation of efficiency of diffractive lenses for wide spectral bandwidth," Opt. Commun. **338**, 54–57 (2015).
8. H. Yang, C. Xue, C. Li, and J. Wang, "Optimal design of multilayer diffractive optical elements with effective area method," Appl. Opt. **55**, 1675–1682 (2016).
9. C. Yang, H. Yang, C. Li, and C. Xue, "Optimization and analysis of infrared multilayer diffractive optical elements with finite feature sizes," Appl. Opt. **58**, 2589–2595 (2019).
10. G. J. Swanson, "Binary optics technology: theoretical limits on the diffraction efficiency of multilevel diffractive optical elements," Tech. Rep. ADA235404 (Lincoln Laboratory/Massachusetts Institute of Technology, 1991).
11. F. Huo, W. Wang, and C. Xue, "Limits of scalar diffraction theory for multilayer diffractive optical elements," Optik **127**, 5688–5694 (2016).
12. V. Laborde, J. Loicq, J. Hastanin, and S. Habraken, "Hybrid ray-tracing/Fourier optics method to analyze multilayer diffractive optical elements," Appl. Opt. **61**, 4956–4966 (2022).
13. V. Laborde, J. Loicq, J. Hastanin, and S. Habraken, "Multilayer diffractive optical element's material selection method based on transmission, total internal reflection and thickness," Appl. Opt. **61**, 7415–7423 (2022).
14. H. Sauer, P. Chavel, and G. Erdei, "Diffractive optical elements in hybrid lenses: modeling and design by zone decomposition," Appl. Opt. **38**, 6482–6486 (1999).
15. A. Nemes-Czopf, D. Bercsényi, and G. Erdei, "Simulation of relief-type diffractive lenses in Zemax using parametric modelling and scalar diffraction," Appl. Opt. **58**, 8931–8942 (2019).
16. C. W. Sweeney and G. E. Sommargren, "Harmonic diffractive lenses," Appl. Opt. **34**, 2469–2475 (1995).
17. D. Faklis and G. M. Morris, "Spectral properties of multiorder diffractive lenses," Appl. Opt. **34**, 2462–2468 (1995).
18. J. W. Goodman, "The angular spectrum of plane waves," in *Introduction to Fourier Optics* (McGraw-Hill, 1996).
19. K. Matsushima and T. Shimobaba, "Band-limited angular spectrum method for numerical simulation of free-space propagation in far and near fields," Opt. Express **17**, 19662–19673 (2009).
20. Breault Research Organization, "ASAPNextGen," 2022, https://breault.com/asap/.
21. OptiwavePhotonic Software, "OptiFDTD," 2022, https://optiwave.com/optifdtd-overview/.
22. SCHOTT, "Reliable solutions for the infrared industry," 2022, https://www.schott.com/en-id/products/ir-materials-p1000261/product-variants.